Numerical Simulation in Applied Geophysics. From the Mesoscale to the Macroscale.

9th China National Symposium on Reservoir Acoustics and Drilling Exploration Technology Frontiers. November 6th 2018

Juan E. Santos,

Universidad de Buenos Aires (UBA), Instituto del Gas y del Petróleo (IGPUBA), Argentina, and Department of Mathematics, Purdue University, West Lafayette, Indiana, USA.

Collaborators: P. M. Gauzellino and Robiel Martínez Corredor, Universidad Nacional de La Plata,

June 1, 2019

Seismic Waves in Hydrocarbon Reservoir Formations. I

- Hydrocarbon Reservoir Formations are fluid-saturated poroelastic media.
- Seismic waves generated near the earth surface or inside wells are used to detect and characterize these formations.
- M. Biot (1956, 1975,1962), presented a theory to describe the propagation of waves in a fluid-saturated poroelastic medium (a Biot medium).
- Biot's theory predicts the existence of two compressional waves (one fast (P1) and one slow (P2) and one shear (fast S) wave.

Seismic Waves in Hydrocarbon Reservoir Formations. II

- P1 or S-waves travelling through a Biot medium containing heterogeneities on the order of centimeters (mesoscopic scale) suffer attenuation and dispersion observed in seismic data (mesoscopic loss).
- The mesoscopic loss effect occurs because different regions of the medium may undergo different strains and fluid pressures.
- This in turn induces fluid flow and Biot slow waves (WIFF) causing energy losses and velocity dispersion due to energy transfer between wave modes.

Numerical simulations illustrating the mesoscopic loss mechanism.

- The computational domain is a square of side length 800 m representing a poroelastic rock alternately saturated with gas and water.
- The perturbation is a compressional point source applied to the matrix, located inside the region at $(x_s, y_s) = (400 \text{ m}, 4 \text{ m})$ with (dominant) frequency 20 Hz.
- Biot's equations of motion were solved for 110 temporal frequencies in the interval $(0, 60Hz)$ employing a Finite Element (FE) parallelizable domain decomposition iterative procedure.
- The domain was discretized into square cells of side length $h = 40$ cm. The time domain solution was obtained performing an approximate inverse Fourier transform.

Time histories in a porous rock saturated by gas (top left), water (top right) and periodic gas-water (bottom)

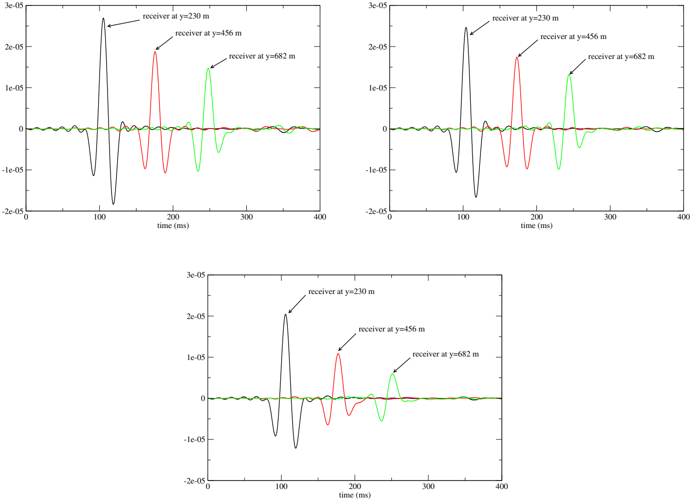

Time histories observed at a receiver for a porous rock saturated by gas, water and periodic gas-water.

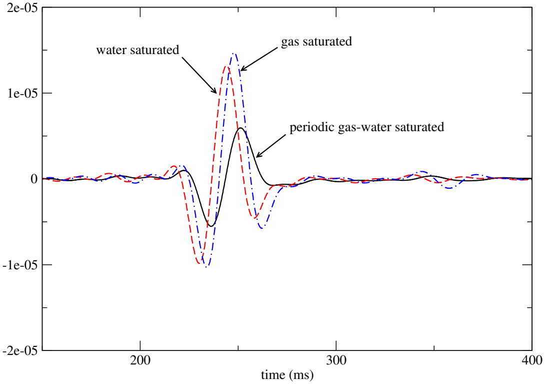

The delay in in the arrival time in the periodic gas-water case is due to the velocity dispersion caused by the mesoscopic scale heterogeneities. The associated attenuation was checked (by computing the numerical Q-factor) to be very good agreement with that predicted by White's theory.

Seismic Waves in Hydrocarbon Reservoir Formations. III

- Since extremely fine meshes are needed to represent mesoscopic-scale heterogeneities, numerical simulations using Biot's equations of motion are computationally expensive or not feasible.
- Alternative: In the context of Numerical Rock Physics, perform compressibility and shear time-harmonic experiments to determine an effective viscoelastic medium long-wave equivalent to a highly heterogeneous Biot medium.
- This effective viscoelastic medium, defined by a plane wave modulus $\overline{E}_u(\omega)$ and a shear modulus $\overline{G}_u(\omega)$, has in the average the same attenuation and velocity dispersion than the highly heterogeneous Biot medium.

Seismic Waves in Hydrocarbon Reservoir Formations. IV

- Each experiment is associated with a Boundary Value Problem (BVP) that is solved using the Finite Element Method (FEM).
- Numerical Rock Physics may, in many circumstances, offer an alternative to laboratory measurements. Numerical experiments are inexpensive and informative since the physical process of wave propagation can be inspected during the experiment.
- Moreover, they are repeatable, essentially free from experimental errors, and may easily be run using alternative models of the rock and fluid properties

Biot's equations in the diffusive range of frequencies.

Frequency-domain stress-strain relations in a Biot medium

$$\tau_{kl}(\mathbf{u}) = 2G\,\epsilon_{kl}(\mathbf{u}^s) + \delta_{kl}\left(\lambda_u\,\nabla\cdot\mathbf{u}^s + B\nabla\cdot\mathbf{u}^f\right),$$
$$p_f(\mathbf{u}) = -B\nabla\cdot\mathbf{u}^s - M\nabla\cdot\mathbf{u}^f,$$

$\mathbf{u} = (\mathbf{u}^s, \mathbf{u}^f)$, $\mathbf{u}^s = (u_1^s, u_3^s), \mathbf{u}^f = (u_1^f, u_3^f)$.

Biot's equations in the diffusive range:

$$\nabla\cdot\tau(\mathbf{u}) = 0,$$
$$\mathrm{i}\omega\mu\kappa^{-1}\mathbf{u}^f + \nabla p_f(\mathbf{u}) = 0,$$

μ: fluid viscosity, κ:frame permeability.

Biot's equations are solved in the 2-D case on a square sample $\Omega = (0, L)^2$ with boundary $\Gamma = \Gamma^L \cup \Gamma^B \cup \Gamma^R \cup \Gamma^T$ in the (x_1, x_3)-plane. The domain Ω is a representative sample of our fluid saturated poroelastic material.

$$\Gamma^L = \{(x_1, x_3) \in \Gamma : x_1 = 0\}, \quad \Gamma^R = \{(x_1, x_3) \in \Gamma : x_1 = L\},$$
$$\Gamma^B = \{(x_1, x_3) \in \Gamma : x_3 = 0\}, \quad \Gamma^T = \{(x_1, x_3) \in \Gamma : x_3 = L\}.$$

For determining the complex plane wave modulus $\overline{E}_u(\omega)$, solve Biot's equations with the boundary conditions

$$\tau(\mathbf{u})\nu \cdot \nu = -\Delta P, \quad (x_1, x_3) \in \Gamma^T,$$
$$\tau(\mathbf{u})\nu \cdot \chi = 0, \quad (x_1, x_3) \in \Gamma,$$
$$\mathbf{u}^s \cdot \nu = 0, \quad (x_1, x_3) \in \Gamma \setminus \Gamma^T,$$
$$\mathbf{u}^f \cdot \nu = 0, \quad (x_1, x_3) \in \Gamma.$$

The complex P-wave modulus of a viscoelastic medium long-wave equivalent to an heterogeneous Biot medium. II

The *equivalent* undrained complex plane-wave modulus $\overline{E_u}(\omega)$ is determined by the relation

$$\frac{\Delta V(\omega)}{V} = -\frac{\Delta P}{\overline{E_u}(\omega)},$$

V: original volume of the sample.
Then to approximate $\Delta V(\omega)$ use

$$\Delta V(\omega) \approx L u_3^{s,T}(\omega).$$

$u_3^{s,T}(\omega)$: average vertical solid displacements $u_3^s(x_1, L, \omega)$ on Γ^T.

For determining the complex shear modulus $\overline{G}_u(\omega)$, solve Biot's equations with the boundary conditions

$$-\tau(\mathbf{u})\nu = \mathbf{g}, \quad (x_1, x_3) \in \Gamma^T \cup \Gamma^L \cup \Gamma^R,$$
$$\mathbf{u}^s = 0, \quad (x, y) \in \Gamma^B,$$
$$\mathbf{u}^f \cdot \nu = 0, \quad (x, y) \in \Gamma,$$

$$\mathbf{g} = \begin{cases} (0, \Delta T), & (x_1, x_3) \in \Gamma^L, \\ (0, -\Delta T), & (x_1, x_3) \in \Gamma^R, \\ (-\Delta T, 0), & (x_1, x_3) \in \Gamma^T. \end{cases}$$

The change in shape of the rock sample allows to recover its *equivalent* complex shear modulus $\overline{G}_u(\omega)$ using the relation

$$\mathrm{tg}(\theta(\omega)) = \frac{\Delta T}{\overline{G}_u(\omega)},$$

$\theta(\omega)$: departure angle from the original positions of the lateral boundaries

The complex shear modulus of a viscoelastic medium long-wave equivalent to an heterogenous Biot medium. II

To find an approximation to $\mathrm{tg}(\theta(\omega))$, compute the average horizontal displacement $u_1^{s,T}(\omega)$ of the horizontal displacements $u_1^s(x_1, L, \omega)$ at the top boundary Γ^T. Then use

$$\mathrm{tg}(\theta(\omega)) \approx u_1^{s,T}(\omega)/L,$$

to determine the shear modulus $\overline{G}_u(\omega)$

Schematic representation of the experiments to determine the complex P-wave and shear modulus

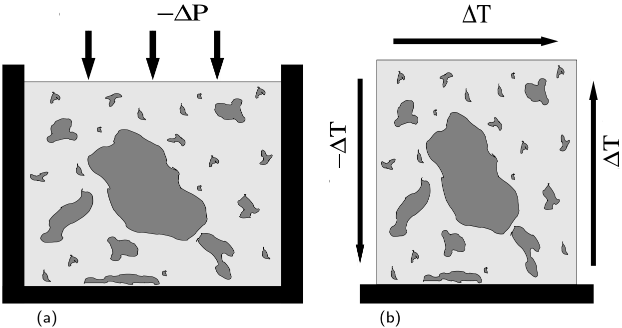

Figures (a) show how to determine $\overline{E}_u(\omega)$, (b) show how to determine $\overline{G}_u(\omega)$.

Variational formulation of the BVP's. I

$$H^{1,P}(\Omega) = \{\mathbf{v} \in [H^1(\Omega)]^2 : \mathbf{v}\cdot\nu = 0 \ \text{ on } \Gamma^L \cup \Gamma^R \cup \Gamma^B\},$$

$$H^{1,T}_{0,B}(\Omega) = \{\mathbf{v} \in [H^1(\Omega)]^2 : \mathbf{v} = 0 \ \text{ on } \Gamma^B\},$$

$$H_0(\mathrm{div},\Omega) = \{\mathbf{v} \in [L^2(\Omega)]^2 : \ \nabla\cdot\mathbf{v} \in L^2(\Omega), \mathbf{v}\cdot\nu = 0 \ \text{ on } \Gamma\}.$$

$$\mathcal{V}^{(P)} = \left[H^{1,P}(\Omega)\right]^2 \times H_0(\mathrm{div};\Omega), \mathcal{V}^{(T)} = \left[H^{1,T}_{0,B}(\Omega)\right]^2 \times H_0(\mathrm{div};\Omega).$$

Let

$$\Lambda(\mathbf{u},\mathbf{v}) = \mathrm{i}\omega\left(\mu\,\kappa^{-1}\mathbf{u}^f,\mathbf{v}^f\right) + \sum_{l,m}\left(\tau_{lm}(\mathbf{u}),\varepsilon_{lm}(\mathbf{v}^s)\right) - \left(p_f(\mathbf{u}),\nabla\cdot\mathbf{v}^f\right)$$

Variational formulation of the BVP's. II

To determine $\overline{E}_u(\omega)$: find $u^{(P)} = (u^{(s,P)}, u^{(f,P)}) \in \mathcal{V}^{(P)}$ such that

$$\Lambda(\mathbf{u}^{(P)}, \mathbf{v}) = -\left\langle \Delta P, \mathbf{v}^s \cdot \nu \right\rangle_{\Gamma^T}, \quad \forall \quad \mathbf{v} = \left(\mathbf{v}^s, \mathbf{v}^f\right) \in \mathcal{V}^{(P)}.$$

To determine $\overline{G}_u(\omega)$: find $\mathbf{u}^{(T)} = (\mathbf{u}^{(s,T)}, \mathbf{u}^{(f,T)}) \in \mathcal{V}^{(T)}$ such that

$$\Lambda(\mathbf{u}^{(T)}, \mathbf{v}) = -\left\langle \mathbf{g}, \mathbf{v}^s \right\rangle_{\Gamma \setminus \Gamma^B}, \qquad \forall \quad \mathbf{v} = \left(\mathbf{v}^s, \mathbf{v}^f\right) \in \mathcal{V}^{(T)}.$$

Finite element procedures. I

$\mathcal{T}^h$: partition of Ω into rectangles R^j of diameter bounded by h.

$$\mathcal{N}^{h,P} = \{\mathbf{v} : \mathbf{v}|_{R^j} \in [P_{1,1}(R^j)]^2, \, \mathbf{v}\cdot\nu = 0 \ \text{on}\ \Gamma^L \cup \Gamma^R \cup \Gamma^B\}$$
$$\mathcal{N}^{h,T}_{0,B} = \{\mathbf{v} : \mathbf{v}|_{R^j} \in [P_{1,1}(R^j)]^2, \, \mathbf{v} = 0 \ \text{on}\ \Gamma^B\} \cap [C^0(\overline{\Omega})]^2.$$
$$\mathcal{V}^h_0 = \{\mathbf{v} : \mathbf{v}|_{R^j} \in P_{1,0} \times P_{0,1}, \, \mathbf{v}\cdot\nu = 0 \ \text{on}\ \Gamma\}.$$
$$\mathcal{V}^{(h,P)} = \mathcal{N}^{h,P} \times \mathcal{V}^h_0, \quad \mathcal{V}^{(h,T)} = \mathcal{N}^{h,T}_{0,B} \times \mathcal{V}^h_0.$$

$P_{s,t}$: polyn. of degree not greater than s in x_1 and not greater than s in x_3.
The FE procedures to determine $\overline{E}_u(\omega)$ and $\overline{G}_u(\omega)$:

$$\Lambda(\mathbf{u}^{(h,P)}, \mathbf{v}) = -\left\langle \Delta P, \mathbf{v}^s \cdot \nu \right\rangle_{\Gamma^T}, \forall\, \mathbf{v} = \left(\mathbf{v}^s, \mathbf{v}^f\right) \in \mathcal{V}^{(h,P)},$$
$$\Lambda(\mathbf{u}^{(h,T)}, \mathbf{v}) = -\left\langle \mathbf{g}, \mathbf{v}^s \right\rangle_{\Gamma\setminus\Gamma^B}, \quad \forall\, \mathbf{v} = \left(\mathbf{v}^s, \mathbf{v}^f\right) \in \mathcal{V}^{(h,T)}.$$

Finite element procedures. II

The mesh size h has to be small enough so that diffusion process associated with the fluid pressure equilibration is accurately resolved.
The diffusion length is given by the relation length

$$L_d = \sqrt{\frac{2\pi\kappa K_f}{\mu\omega}}, \quad K_f = \text{fluid bulk modulus}$$

We take h so that the minimum diffusion length is discretized with at least 3 mesh points at the highest frequency, which is sufficient to represent a (smooth) diffusion-type process.
Besides, the size of the rock sample is not arbitrary: it has to be big enough to constitute a representative part of the Biot medium but, at the same time, it has to be much smaller than the wavelengths associated with each frequency.

Determination of $\overline{E}_u(\omega)$ in patchy gas-brine saturated rocks.

Patchy gas-brine saturation arises in hydrocarbon reservoirs, where regions of non-uniform patchy saturation occur at gas-brine contacts. Patchy-saturation patterns produce very important mesoscopic loss effects at the seismic band of frequencies, as was first shown by J. E. White (GPY, 1975).

To study these effects, consider porous samples with spatially variable gas-brine distribution in the form of irregular patches fully saturated with gas and zones fully saturated with brine. The domain Ω is a square of side length 50 cm, and a 75×75 mesh uniform is used.

Patchy gas-brine distribution for two different correlation lengths. White zones: full gas saturation, black zones: full brine saturation

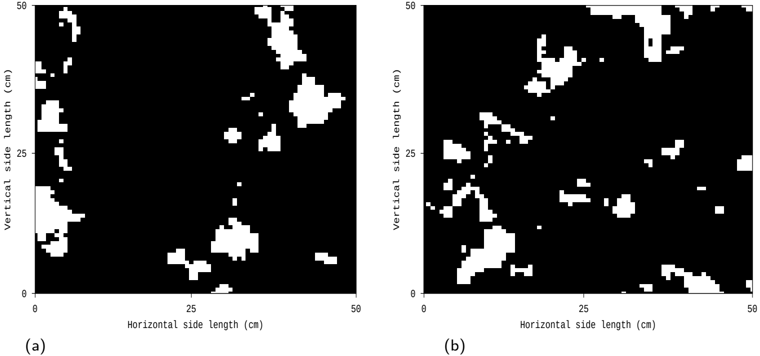

(a): correlation length 10 cm (b): correlation lengths 5 cm.

Compressional phase velocity and inverse quality factors for two different correlation lengths CL

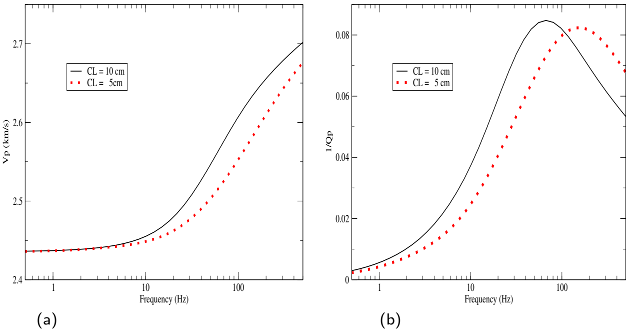

(a): Compressional phase velocity (b): Inverse quality factors. Notice the attenuation peak moving to higher frequencies for the shorter CL.

Pressure distribution (Pa) at two different frequencies.

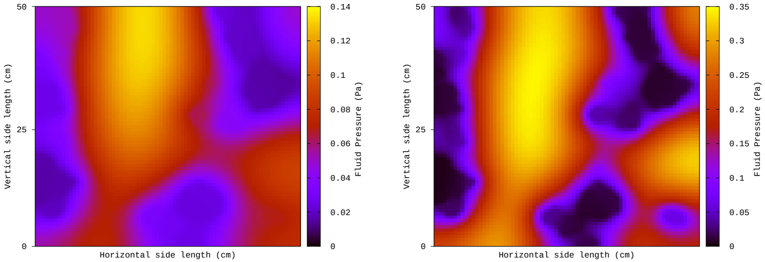

(a) (b)

(a): 10 Hz (b): 60 Hz.

Gradient of pressures can be seen at the gas-water interfaces, stronger at 65 Hz than at 10 Hz. This Figure illustrates the mesoscopic loss mechanism.

The effective shear modulus when the solid matrix is composed of two different materials.

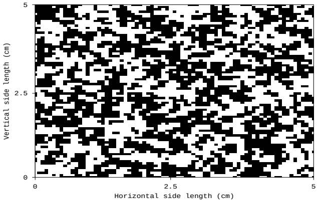

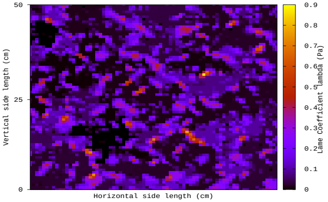

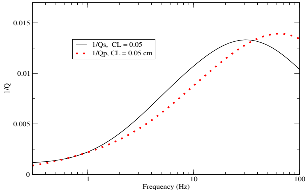

Top left: Fractal shale-sandstone distribution. Black zones correspond to pure shale and white ones to pure sandstone. Shale percentage is 50 %. Top right: Absolute fluid pressure distribution (Pa) at 30 Hz. Bottom: Inverse quality factors Q_s and Q_p. Q_s of about 75 between 20 and 40 Hz, Q_p about 70 at 65 Hz. Conclusion: wave induced fluid flow (mesoscopic loss) is observed when shear and compressional waves propagate through Biot media with highly heterogeneous solid frames.

Fractured Biot media. I

- Fractures are common in the earth's crust due to different factors, for instance, tectonic stresses and natural or artificial hydraulic fracturing caused by a pressurized fluid.
- Seismic wave propagation through fractures and cracks is an important subject in exploration and production geophysics, earthquake seismology and mining.
- Fractures constitute the sources of earthquakes, and hydrocarbon and geothermal reservoirs are mainly composed of fractured rocks .

Fractured Biot media. II

- Modeling fractures requires a suitable interface model. Nakagawa and Schoenberg (JASA (2007)) presented a set of boundary conditions (B.C.) to represent fluid-solid interaction within a fracture and the effect of its permeability on seismic wave scattering.
- At a fracture, these B.C. impose: continuity of the total stress components, discontinuity of pressure proportional to averaged fluid velocities and discontinuities of displacements proportional to stress components and averaged fluid pressures.
- They allow to represent wave-induced fluid flow (mesoscopic loss) by which the fast waves are converted to slow (diffusive) Biot waves when travelling across fractures.

Boundary conditions at a fracture within a Biot medium in terms of fracture compliances. I

$\Omega = (0, L_1) \times (0, L_3)$ with boundary Γ in the (x_1, x_3)-plane, x_1, x_3: horizontal and vertical coordinates, respectively.

Ω contains a set of horizontal fractures $\Gamma^{(f,l)}, l = 1, \cdots, J^{(f)}$ each one of length L_1 and aperture $h^{(f)}$. This set of fractures divides Ω in a collection of non-overlapping rectangles $R^{(l)}, l = 1, \cdots, J^f + 1$.

Assume that the rectangles $R^{(l)}$ and $R^{(l+1)}$ have a fracture $\Gamma^{(f,l)}$ as a common side.

$[\mathbf{u}^s], [\mathbf{u}^f]$: jumps of the solid and fluid displacement vectors at $\Gamma^{(f,l)}$.

$\nu_{l,l+1}$ and $\chi_{l,l+1}$: the unit outer normal and a unit tangent (oriented counterclockwise) on $\Gamma^{(f,l)}$ from $R^{(l)}$ to $R^{(l+1)}$.

Boundary conditions at a fracture $\Gamma^{(f,l)}$ within a Biot medium in terms of fracture compliances. II

$$[\mathbf{u}^s \cdot \nu_{l,l+1}] = \eta_N \Big((1 - \alpha^{(f)} \widetilde{B}^{(f)} (1 - \Pi)) \tau(\mathbf{u}) \nu_{l,l+1} \cdot \nu_{l,l+1} - \alpha^{(f)} \frac{1}{2} \left((-p_f^{(l+1)}) + (-p_f^{(l)}) \right) \Pi \Big),$$

$$[\mathbf{u}^s \cdot \chi_{l,l+1}] = \eta_T \, \tau(\mathbf{u}) \nu_{l,l+1} \cdot \chi_{l,l+1},$$

$$\left[\mathbf{u}^f \cdot \nu_{l,l+1}\right] = \alpha^{(f)} \eta_N \Big(-\tau(\mathbf{u}) \nu_{l,l+1} \cdot \nu_{l,l+1} + \frac{1}{\widetilde{B}^{(f)}} \frac{1}{2} \left((-p_f^{(l+1)}) + (-p_f^{(l)}) \right) \Big) \Pi,$$

$$(-p_f^{(l+1)}) - (-p_f^{(l)}) = \frac{\mathrm{i} \varnothing \mu^{(\mathrm{f})\,\prime\prime}}{\widehat{\kappa}^{(f)}} \frac{1}{2} \left(\mathbf{u}_f^{(l+1)} + \mathbf{u}_f^{(l)} \right) \cdot \nu_{l,l+1},$$

$$\tau(\mathbf{u}) \nu_{l,l+1} \cdot \nu_{l,l+1} = \tau(\mathbf{u}) \nu_{l+1,l} \cdot \nu_{l+1,l},$$

$$\tau(\mathbf{u}) \nu_{l,l+1} \cdot \chi_{l,l+1} = \tau(\mathbf{u}) \nu_{l+1,l} \cdot \chi_{l+1,l},$$

η_N and η_T: normal and tangential fracture compliances.

Fracture dry plane wave and shear modulus $H_m^{(f)} = K_m^{(f)} + \frac{4}{3}G^{(f)}$ and $G^{(f)}$ are defined in terms of fracture compliances η_N, η_T and fracture aperture $h^{(f)}$:

$$\eta_N = \frac{h^{(f)}}{H_m^{(f)}}, \qquad \eta_T = \frac{h^{(f)}}{G^{(f)}}.$$

$$\alpha^{(f)} = 1 - \frac{K_m^{(f)}}{K_s^{(f)}}, \qquad \widehat{\kappa}^{(f)} = \frac{\kappa^{(f)}}{h^{(f)}},$$

$$\epsilon = \frac{(1+\mathrm{i})}{2}\left(\frac{\varnothing\,\eta^{(f)}\,\alpha^{(f)}\,\eta_N}{2\,\widetilde{B}^{(f)}\,\widehat{\kappa}^{(f)}}\right)^{1/2}, \quad \Pi(\epsilon) = \frac{\tanh\epsilon}{\epsilon},$$

$$\widetilde{B}^{(f)} = \frac{\alpha^{(f)}M^{(f)}}{H_u^{(f)}}, \quad H_u^{(f)} = K_u^{(f)} + \frac{4}{3}G^{(f)}.$$

$K_u^{(f)}$: undrained fracture bulk modulus

A VTI medium equivalent to a Biot's medium with aligned fractures. I

- A Biot medium with a dense set of horizontal fractures behaves as a Viscoelastic Transversely Isotropic (VTI) medium when the average fracture distance is much smaller than the predominant wavelength of the travelling waves.
- This leads to frequency and angular variations of velocity and attenuation of seismic waves.
- The time-harmonic experiments described before are generalized and applied to determine the VTI medium long-wave equivalent to a densely fractured Biot medium.

A VTI medium equivalent to a Biot's medium with aligned fractures. II

$\widetilde{\sigma}_{ij}(\widetilde{\vec{u}}^s)$, $e_{ij}(\widetilde{\vec{u}}^s)$: stress and strain tensor components of the equivalent VTI medium

$\widetilde{\vec{u}}^s$: solid displacement vector at the macro-scale.

The TIV stress-strain relations:

$$
\begin{aligned}
\widetilde{\sigma}_{11}(\widetilde{\vec{u}}^s) &= p_{11}\ e_{11}(\widetilde{\vec{u}}^s) + p_{12}\ e_{22}(\widetilde{\vec{u}}^s) + p_{13}\ e_{33}(\widetilde{\vec{u}}^s),\\
\widetilde{\sigma}_{22}(\widetilde{\vec{u}}^s) &= p_{12}\ e_{11}(\widetilde{\vec{u}}^s) + p_{11}\ e_{22}(\widetilde{\vec{u}}^s) + p_{13}\ e_{33}(\widetilde{\vec{u}}^s),\\
\widetilde{\sigma}_{33}(\widetilde{\vec{u}}^s) &= p_{13}\ e_{11}(\widetilde{\vec{u}}^s) + p_{13}\ e_{22}(\widetilde{\vec{u}}^s) + p_{33}\ e_{33}(\widetilde{\vec{u}}^s),\\
\widetilde{\sigma}_{23}(\widetilde{\vec{u}}^s) &= 2\ p_{55}\ e_{23}(\widetilde{\vec{u}}^s),\\
\widetilde{\sigma}_{13}(\widetilde{\vec{u}}^s) &= 2\ p_{55}\ e_{13}(\widetilde{\vec{u}}^s),\\
\widetilde{\sigma}_{12}(\widetilde{\vec{u}}^s) &= 2\ p_{66}\ e_{12}(\widetilde{\vec{u}}^s).
\end{aligned}
$$

$$p_{22} = p_{11}, \quad p_{23} = p_{13}, \quad p_{55} = p_{44}, p_{12} = p_{11} - 2p_{66}.$$

A VTI medium equivalent to a Biot's medium with aligned fractures. III

- In the context of Numerical Rock Physics the complex stiffness coefficients $p_{IJ}(\omega)$ are determined using five time-harmonic experiments, each one associated with a BVP.
- The BVP's consist on compressibility and shear tests on a sample of Biot material with a dense set of fractures modeled using B. C..
- The BVP's are formulated in the space-frequency domain and solved using th FEM.

The Experiments to Determine the Five TIV Stiffness p_{IJ}

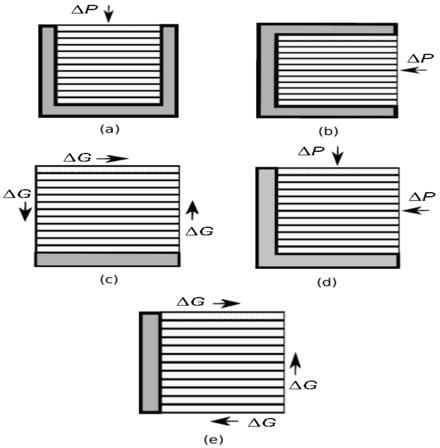

(I) : Figures (a) and (b) show how to determine p_{33} and p_{11}, (c) determines p_{55}, (e) determines p_{66}, (d) determines p_{13}.

Numerical Experiments. I

The procedure to determine the complex stiffnesses $p_{IJ}(\omega)$ at the macro-scale was validated by comparison with the analytical solution given by Krzikalla and Müller (GPY, 2011).

Next it was applied to patchy brine-gas saturation, a case for which no analytical solutions are avalaible.

Instead of the stiffnesses $p_{IJ}(\omega)$ the Figures display the the corresponding energy velocities and dissipation coefficients.

In all the experiments we used square samples of side length 2 m, with 9 fractures at equal distance of 20 cm and fracture aperture $h^{(f)} = 1$ mm.

The numerical samples were discretized with a 100×100 uniform mesh.

Material Properties of background and fractures.

Table: Material properties of background and fractures

Background	Solid grains bulk modulus, K_s	36. GPa
	solid grains density, ρ_s	2700 kg/m^3
	Dry bulk modulus K_m	9 GPa
	shear modulus G	7 GPa
	Porosity ϕ	0.15
	permeability κ	0.1 Darcy
Fractures	Solid grains bulk modulus, K_s	36. GPa
	solid grains density, ρ_s	2700 kg/m^3
	Dry bulk modulus K_m	0.0055 GPa
	shear modulus G	0.0033 GPa
	Porosity ϕ	0.5
	permeability κ	10 Darcy

qP and qSV energy velocity at 30 Hz for full brine, full gas, 10% and 50% patchy gas-brine saturation.

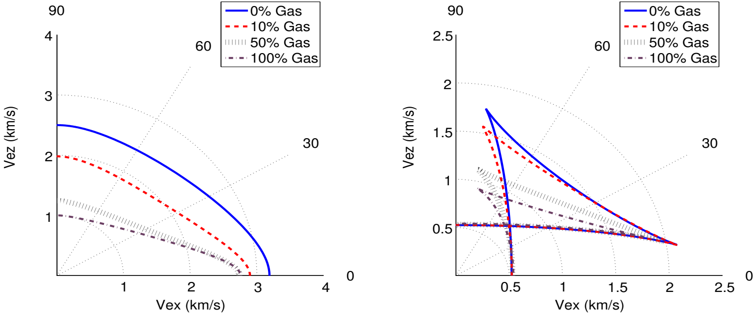

(a) : qP energy velocity (b) : qSV energy velocity.

qP and qSV velocity decreases as gas saturation increases. qSV velocity exhibits the typical cuspidal triangles.

Numerical Simulation in Applied Geophysics. From the Mesoscale to the Macroscale.

Juan E. Santos,

qP and qSV dissipation factors at 30 Hz for full brine, full gas, 10% and 50% patchy gas-brine saturation.

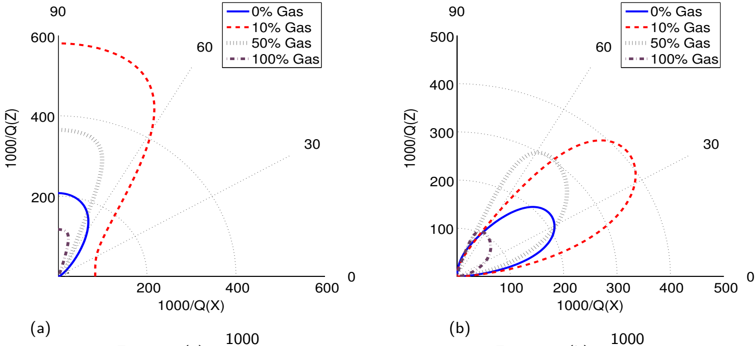

Figure 36(a) : $\frac{1000}{qP}$ Figure 36 (b) : $\frac{1000}{qSV}$.

qP anisotropy is enhanced by patchy saturation, is highest at 10 % gas saturation and with maximums for waves arriving normally to the fracture layering. qSV waves show maximum attenuation at 10 % gas saturation, with different anisotropic behavior depending on gas saturation.

SH energy velocity at 30 Hz for full brine saturation. The SH polarization is normal to the plane (x_1, x_3) that is the plane of the figure

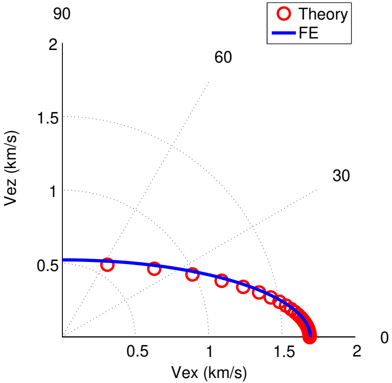

SH waves show velocity anisotropy and they are lossless

Fluid pressure for normal compression to the fractures at 30 Hz and 10 % patchy gas-brine saturation.

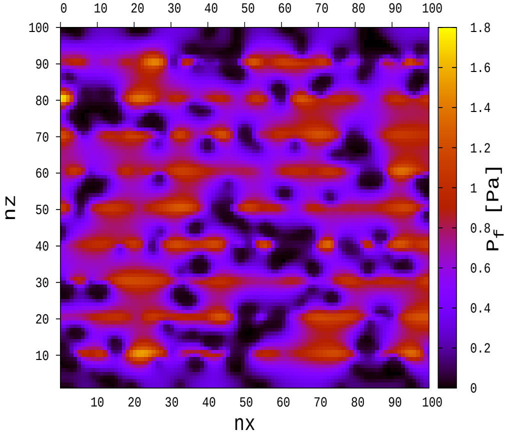

Higher pressure values occur at fractures. Darker regions identify gas patches. High pressure gradients at boundaries of fractures and patches show the mesoscopic loss effect.

Upscaling of 3D Biot media with a dense sets of horizontal and vertical fractures

- This part of the presentation describes two procedures to model the acoustic response of fluid saturated poroelastic media with dense sets of horizontal an vertical fractures.
- The procedures use generalizations of the harmonic experiments to obtain a viscoelastic medium long-wave equivalent to a fractured fluid-saturated poroelastic medium.

Representative sample of a Biot medium with a dense set of horizontal and vertical fractures.

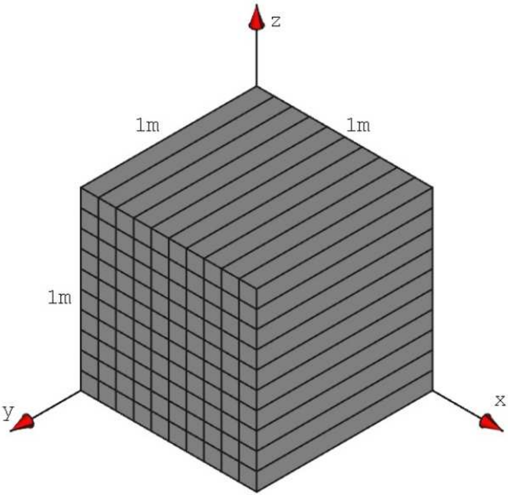

Fluid-saturated fractured poroelastic sample.

The long-wave equivalent orthorhombic medium. I

- Numerical simulations of wave propagation in this type of fractured porous medium requires very fine meshes, since fracture apertures are on the order of mm to cm.
- To overcome this difficulty we determine a viscoelastic orthorhombic medium long-wave equivalent to the fractured Biot medium using two approaches.
- The first approach (the Helbig-Schoenberg or H-S model) uses a set of harmonic experiments on samples of a horizontally fractured Biot media to determine a VTI background where later the vertical fractures are included.
- The second approach uses a collection of harmonic experiments to determine the nine stiffness coefficients of the long-wave equivalent orthorhombic medium.

The long-wave equivalent orthorhombic medium using the H-S model. II

First we determine a viscoelastic transversely isotropic (VTI) background with vertical axis of symmetry.
The five complex and frequency dependent stiffness c_{IJ} of the equivalent (VTI) background medium associated with the set of horizontal fractures are determined using the five harmonic experiments described before.
These coefficients define a stiffness matrix $C(\omega) = \mathrm{Re}(C(\omega)) + \mathrm{i}\,\mathrm{Im}(C(\omega))$ that represents the stress-strain relations in the space-frequency domain.
$\mathrm{Re}(C(\omega))$ must be positive definite because represents the strain energy, while the positive definitess of $\mathrm{Im}(C(\omega))$ is imposed by the First and Second Thermodynamic Laws.

The long-wave equivalent orthorhombic medium using the H-S model. III

The VTI matrix is

$$
C(\omega) = \begin{pmatrix}
c_{11}(\omega) & c_{12}(\omega) & c_{13}(\omega) & 0 & 0 & 0 \\
c_{12}(\omega) & c_{11}(\omega) & c_{13}(\omega) & 0 & 0 & 0 \\
c_{13}(\omega) & c_{13}(\omega) & c_{33}(\omega) & 0 & 0 & 0 \\
0 & 0 & 0 & c_{55}(\omega) & 0 & 0 \\
0 & 0 & 0 & 0 & c_{55}(\omega) & 0 \\
0 & 0 & 0 & 0 & 0 & c_{66}(\omega)
\end{pmatrix}
$$

where,

$$
c_{12}(\omega) = c_{11}(\omega) - 2c_{66}(\omega).
$$

The equivalent viscoelastic orthorhrombic medium using the H-S model. IV

Vertical fractures are included in the VTI background to obtain an orthorhombic medium at the macroscale using the model proposed by Schoenberg and Helbig (GPY, 1997) and later generalized by Carcione et al. (RMRE, 2012).

The Schoenberg-Helbig model modifies the VTI matrix stiffness $C(\omega)$ using complex compliances oriented in the the x_2 axes to determine an orthorhombic matrix $P_(\omega)$

It was verified that both $\mathrm{Re}(P(\omega))$ and $\mathrm{Im}(P(\omega))$ remain positive definite after applying this modification.

This orthorhombic model allows to take into account mesoscopic attenuation due to wave-induced fluid flow (WIFF), by which the fast waves are converted to slow Biot waves when travelling across fractures.

The equivalent viscoelastic orthorhrombic medium using the H-S model. IV

The set of fractures oriented along the x_2-axes is represented by the compliance matrix

$$\mathbf{S_f} = \begin{pmatrix} Z_N & 0 & 0 & 0 & 0 & 0 \\ 0 & 0 & 0 & 0 & 0 & 0 \\ 0 & 0 & 0 & 0 & 0 & 0 \\ 0 & 0 & 0 & 0 & 0 & 0 \\ 0 & 0 & 0 & 0 & Z_V & 0 \\ 0 & 0 & 0 & 0 & 0 & Z_H \end{pmatrix}$$

The compliances can be expressed as

$$Z_N = \frac{1}{\kappa_N + i\omega\eta_N}, \quad Z_H = \frac{1}{\kappa_H + i\omega\eta_H}, \quad Z_V = \frac{1}{\kappa_V + i\omega\eta_V}, \tag{1}$$

$\kappa_N = L\kappa_1$, $\kappa_H = L\kappa_2$ and $\kappa_V = L\kappa_3$, $\eta_N = L\eta_1$, $\eta_H = L\eta_2$, $\eta_V = L\eta_3$.
L: average fracture spacing.

The complex stiffness defining the elements of the orthorhombic matrix using the H-S model

$$
\begin{aligned}
p_{11}(\omega) &= c_{11}(\omega)(1-\delta_N),\\
p_{12}(\omega) &= c_{12}(\omega)(1-\delta_N),\\
p_{13}(\omega) &= c_{13}(\omega)(1-\delta_N),\\
p_{22}(\omega) &= c_{11}(\omega)(1-\delta_N c_{12}^2(\omega)/c_{11}^2(\omega)),\\
p_{23}(\omega) &= c_{13}(\omega)(1-\delta_N c_{12}^2(\omega)/c_{11}^2(\omega)),\\
p_{33}(\omega) &= c_{33}(\omega)[1-\delta_N c_{13}^2(\omega)/(c_{11}(\omega)c_{33}(\omega))],\\
p_{44}(\omega) &= c_{55}(\omega),\\
p_{55}(\omega) &= c_{55}(\omega)(1-\delta_V),\\
p_{66}(\omega) &= c_{66}(\omega)(1-\delta_H).
\end{aligned}
$$

Here

$$
\delta_N = \frac{Z_N c_{11}(\omega)}{1+Z_N c_{11}(\omega)}, \quad \delta_V = \frac{Z_V c_{55}(\omega)}{1+Z_V c_{55}(\omega)}, \quad \delta_H = \frac{Z_H c_{66}(\omega)}{1+Z_H c_{66}(\omega)}. \tag{2}
$$

If $\omega = 0$, the elements of (2) correspond to the stiffness matrix of Schoenberg-Helbig, GPY, 1997.

Consider the simulation of seismic wave propagation in a gas-brine saturated fractured porous material with high fracture intensity, 20 horizontal fractures per meter and fracture aperture 1cm.

Porosity and permeability: $\phi = 0.25, \kappa = 0.247$ Darcy in the background, $\phi = 0.5, \kappa = 2.5$ Darcy in the fractures.

Dry bulk and shear modulus: $K_m = 11.7$ GPa, $\mu_m = 14$ GPa in the background, $K_m = 0.58$ GPa, $\mu_m = 0.68$ GPa in the fractures.

Fracture compliances in the x_2-direction:

$$Z_N = \frac{1}{\kappa_N + i\omega\eta_N} \quad Z_H = \frac{1/}{\kappa_H + i\omega\eta_H} \quad Z_V = \frac{1}{\kappa_V + i\omega\eta_V}$$

$$\kappa_N = 9\,\mathrm{Real}(c_{11}(\omega))\kappa_H = 5.66\,\mathrm{Real}(c_{66}(\omega)) \quad \kappa_V = 5.66\,\mathrm{Real}(c_{55}(\omega))$$

$$\eta_N = \alpha\kappa_N, \quad \eta_H = \alpha\kappa_H, \quad \eta_V = \alpha\kappa_V, \quad \alpha = 10^{-3}$$

Stiffness coefficients of the orthorhormbic and VTI equivalent media (GPa) at 35 Hz using the H-S model.

ORTHORHOMBIC H-S model	$p_{11}(\omega)$	(22.00, 0.55)
	$p_{22}(\omega)$	(24.33, 0.084)
	$p_{33}(\omega)$	(6.40, 0.32)
	$p_{44}(\omega)$	(2.87, 0.0)
	$p_{55}(\omega)$	(2.45, 0.08)
	$p_{66}(\omega)$	(9.60, 0.3)
	$p_{12}(\omega)$	(1.70, 0.1
	$p_{13}(\omega)$	(0.59, 0.2)
	$p_{23}(\omega)$	(0.65, 0.016)
VTI background	$p_{11}(\omega)$	(24.34, 0.003)
	$p_{33}(\omega)$	(6.45,0.0001)
	$p_{55}(\omega)$	(2.87,0.0)
	$p_{66}(\omega)$	(11.23, 0.4 10^{-6})
	$p_{13}(\omega)$	(0.66, 0.0005)

Energy velocities of qP, qSV and SH waves on the planes (x, z) (x, y) and (y, z) at 30 Hz. H-S model

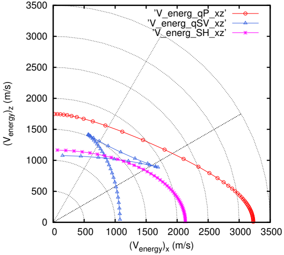

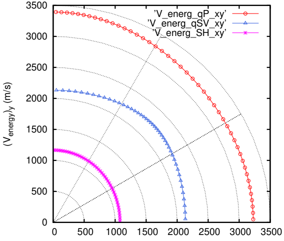

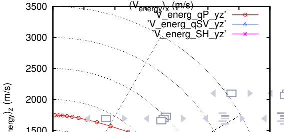

Attenuation coefficient of qP, qSV and SH waves on the planes (x, z) (x, y) and (y, z) at 30 Hz. H-S model

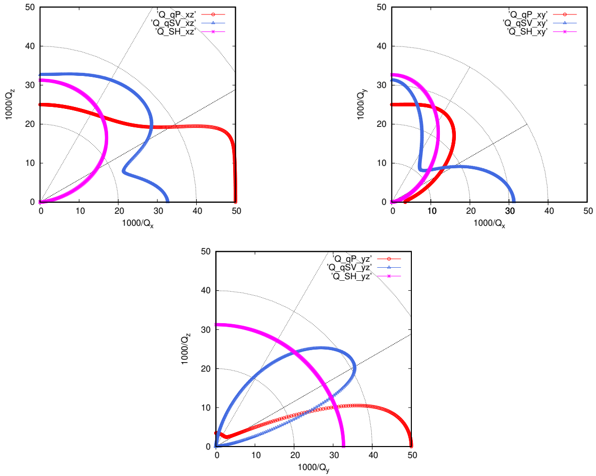

Top left: Attenuation coefficient in the vertical plane (x, z). Top right: Attenuation coefficient in the horizontal plane (x, y). Bottom: Attenuation coefficient in the vertical plane (y, z).

qP, qSV and SH waves show attenuation anisotropy in all planes

Wave propagation in the equivalent orthorhombic medium using the H-S model. Snapshots at 160 ms on the (x, z)-plane

The computational domain is a cube of side length 1120 m. Mesh size is 224 × 224 × 224. Waves are generated by a point source of principal frequency 30 Hz located at the center of the domain.

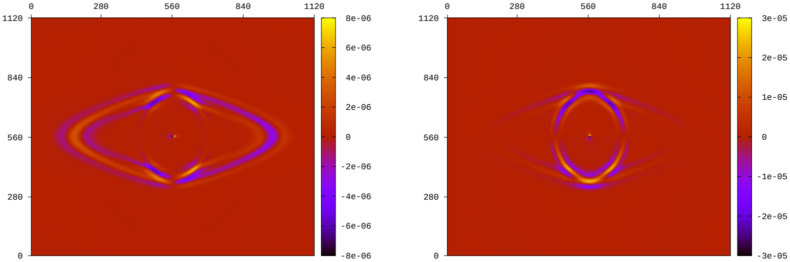

(a) (b)

a) Horizontal component of the displacement b) vertical component of the displacement.

The exterior wave front corresponds to the qP wave, while the interior one is a qSV wavefront.

Wave propagation in the equivalent orthorhombic medium using the H-S model. Snapshots at 160 ms on the (x, y)-plane

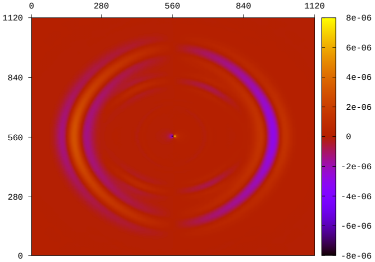

(a)

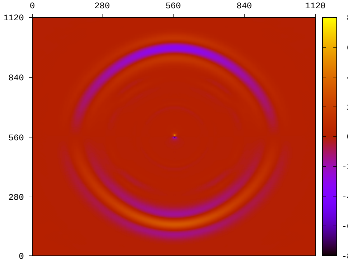

(b)

a) Horizontal x-component of the displacement b) Horizontal y-component of the displacement.
The wave fronts are almost isotropic as indicated in the polar plots of the energy velocities in the (x, y)-plane.
The fast wavefronts in a) and b) correspond to the qP wave. The slow wavefront of the horizontal x-component corresponds to a slow shear wave traveling across the normal fractures in the (y, z)-plane.
Finally , the slow wavefront of the horizontal y-component is a fast shear wave travelling along the fractures.

Wave propagation in the equivalent orthorhombic medium using the H-S model . Snapshots at 160 ms on the (y, z)-plane

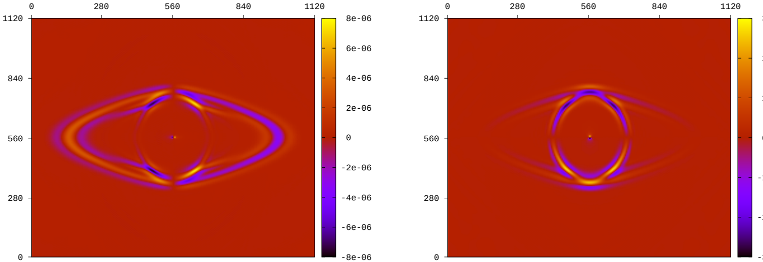

(a) (b)

a) Horizontal component of the displacement b) vertical component of the displacement.

The exterior wave front corresponds to the qP wave, while the interior one is a qSV wavefront.

The second approach. The harmonic experiments to determine an effective orthorhombic medium. I

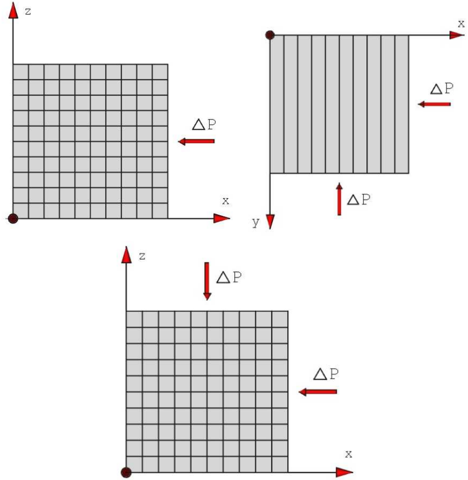

Top left: determines p_{11}, Top right: determines p_{12}, Bottom: determines p_{13}.

The harmonic experiments to determine an effective orthorhombic medium. II

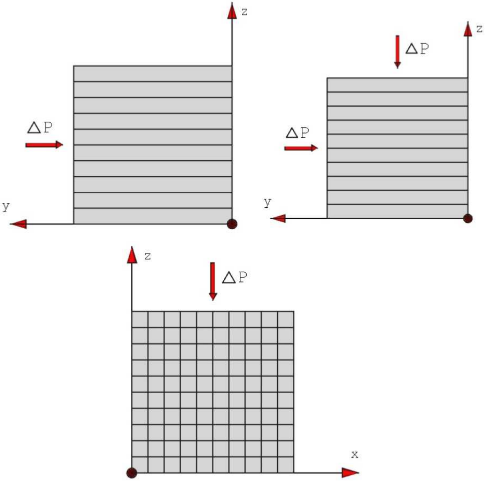

Top left: determines p_{22}, Top right: determines p_{23}, Bottom: determines p_{33}.

The harmonic experiments to determine an effective orthorhombic medium. III

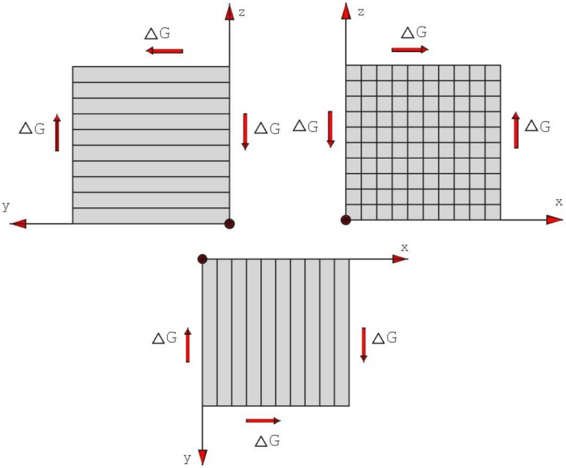

Top left: determines p_{44}, Top right: determines p_{55}, Bottom: determines p_{66}.

Energy velocities of qP, qSV and SH waves on the planes (x, z) (x, y) and (y, z) at 30 Hz determined using the p_{IJ} from the harmonic experiments. Both background and fractures are brine saturated.

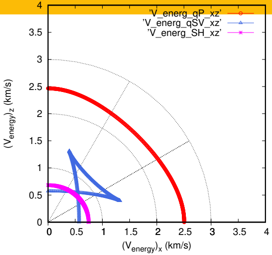

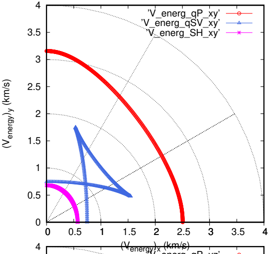

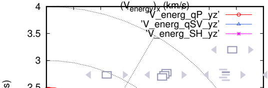

Attenuation coefficient of qP, qSV and SH waves on the planes (x, z) (x, y) and (y, z) at 30 Hz determined using the p_{IJ} from the harmonic experiments. Both background and fractures are brine saturated

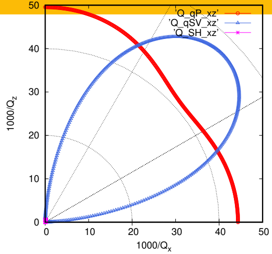

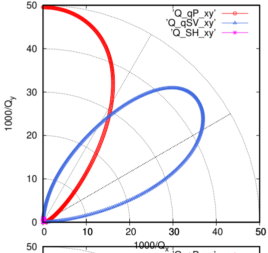

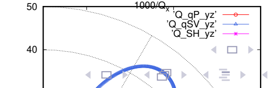

The VSP experiment. An orthorhombic layer inside isotropic layers

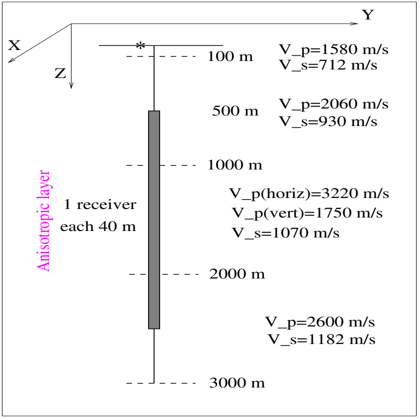

The source is a force in the vertical direction

Traces of the particle velocity in the VSP experiment

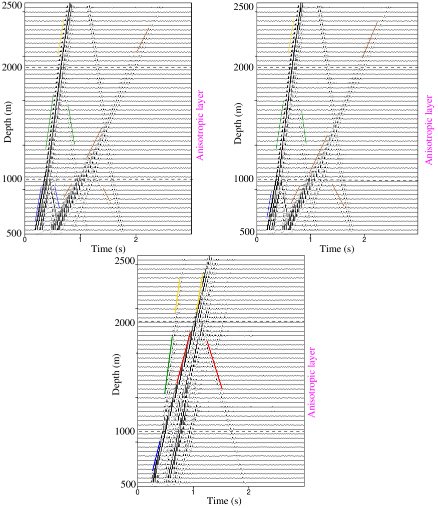

Top left: x-component of displacement Top right: y-component of displacement Bottom: z-component of displacement.

Blue line: P wave trans. in the 2nd layer. Green line: qP wave trans. in the 3rd orthorhombic layer. Yellow line: P wave trans. in the 4th layer. Pink line: trans. shear waves S or qSV. Red line in z-component: qP trans. in 3rd orthorhombic layer. Opposite slops indicate reflected P, qP or S waves.

Traces from the x-component of the particle velocity in the VSP experiment.

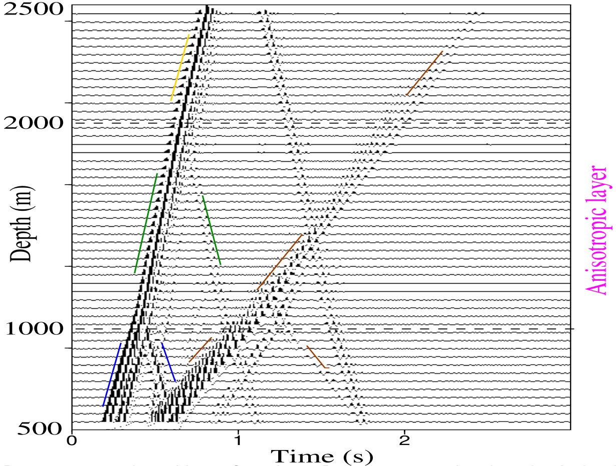

Blue line: P wave trans. in the 2nd layer. Green line: qP wave transmitted in the 3rd orthorhombic layer.

Yellow line: P wave transmitted in the 4th layer. Pink line: transmitted . shear S or qSV waves. The

opposite slops are reflected P, qP or S waves.

Traces from the y-component of the particle velocity in the VSP experiment.

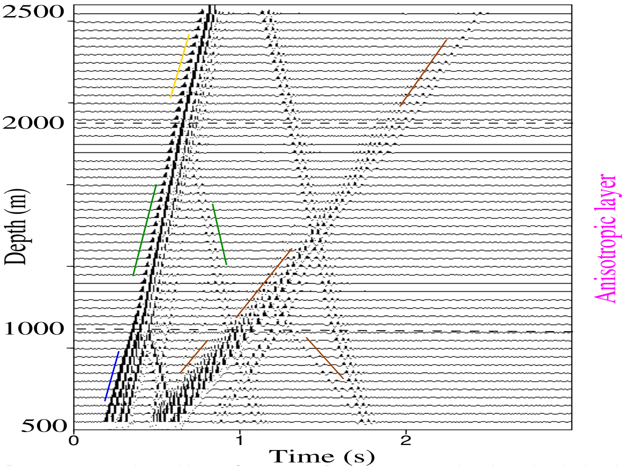

Blue line: P wave trans. in the 2nd layer. Green line: qP wave transmitted in the 3rd orthorhombic layer. Yellow line: P wave transmitted in the 4th layer. Pink line: transmitted . shear S or qSV waves. The opposite slops indicate reflected P, qP or S waves.

Traces from the z-component of the particle velocity in the VSP experiment.

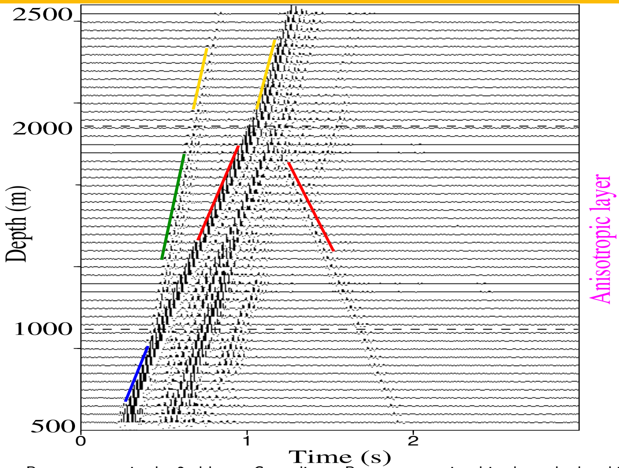

Blue line: P wave trans. in the 2nd layer. Green line: qP wave transmitted in the orthorhombic layer. Yellow line: P wave transmitted in the 4th layer. Pink line: transmitted . shear S or qSV waves. Red line: qP transmitted in orthorhombic layer with vertical velocity 1750 m/s Opposite slops indicate reflected P, qP or S waves.

Numerical Simulation in Applied Geophysics. From the Mesoscale to the Macroscale.

Thanks for your attention !!!!